ACS Catalysis

Research Article

pubs.acs.org/acscatalysis

Pyrolyzed Fe–N–C Composite as an Efficient Non-precious Metal Catalyst for Oxygen Reduction Reaction in Acidic Medium

Mei-Qing Wang,[†] Wei-Hua Yang,*[,†] Hong-Hui Wang,[‡] Chi Chen,[§] Zhi-You Zhou,[‡] and Shi-Gang Sun*[,‡]

[†]College of Materials Science and Engineering, Huaqiao University, Xiamen, Fujian 361021, People's Republic of China

[‡]State Key Laboratory of Physical Chemistry of Solid Surfaces, Department of Chemistry, College of Chemistry and Chemical Engineering, Xiamen University, Xiamen, Fujian 361005, People's Republic of China

[§]State Key Laboratory of Chemical Engineering, East China University of Science and Technology, Shanghai 200237, People's Republic of China

Supporting Information

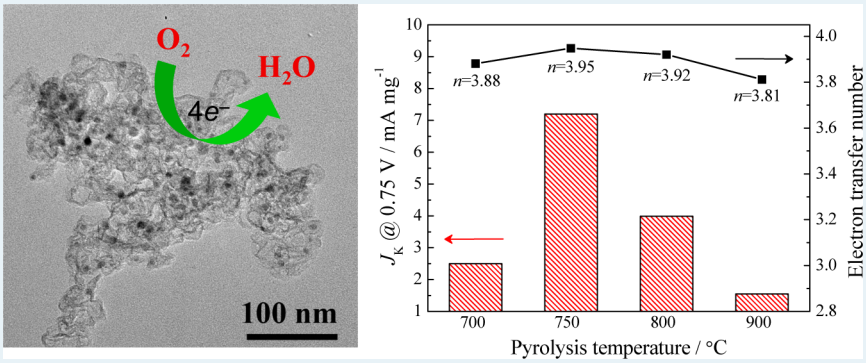

ABSTRACT: Aimed at developing a highly active and stable non-precious metal catalyst (NPMC) for oxygen reduction reaction (ORR) in acidic proton-exchange membrane fuel cells (PEMFCs), a novel NPMC was prepared by pyrolyzing a composite of carbon-supported Fe-doped graphitic carbon nitride (Fe–g-C_3N_4@C) above 700 °C. In this paper, the influence of the pyrolysis temperature and Fe content on ORR performance was investigated. Rotating disk electrode (RDE) and rotating ring-disk electrode (RRDE) studies reveal that, with a half-wave potential of 0.75 V [versus reversible hydrogen electrode (RHE)] and a H_2O_2 yield of 2.6% at 0.4 V, the as-synthesized catalyst heat-treated at 750 °C with a Fe salt/dicyandiamide (DCD) mass ratio of 10% displays the optimal ORR activity and selectivity. Furthermore, the pyrolyzed Fe–N–C composite exhibits superior durability in comparison to that of commercial 20 wt % Pt/C in acidic medium, making it a good candidate for an ORR electrocatalyst in PEMFCs.

KEYWORDS: *non-precious metal catalyst (NPMC), oxygen reduction reaction (ORR), proton-exchange membrane fuel cell (PEMFC), carbon-supported Fe-doped g-C_3N_4 (Fe–g-C_3N_4@C), pyrolysis, Fe–N–C composite*

1. INTRODUCTION

Proton-exchange membrane fuel cells (PEMFCs) are considered as one of the most promising power source candidates for transport, stationary, and portable applications because of their high energy density, high overall energy conversion efficiency, and low emissions.[1,2] Platinum (Pt)-based materials[3−5] have long been regarded as the most effective catalysts for the hydrogen oxidation reaction (HOR) and oxygen reduction reaction (ORR) at the anode and cathode of PEMFCs, respectively. However, the sluggish kinetics of ORR results in serious cathode polarization and energy loss. Furthermore, the prohibitive cost, limited storage, and poor durability of Pt have significantly hindered the commercialization of PEMFCs.[6] Consequently, as alternative materials, the development of non-precious metal catalysts (NPMCs) with high activity and long-term durability for ORR is highly beneficial to reduce the cost and promote the commercialization of PEMFCs.

Transition metal–nitrogen-containing complexes supported on carbon materials (M–N/C, where M = Fe and Co) are considered to be the most promising NPMCs for replacing Pt.[7−9] The synthesis of this kind of NPMC was through heat treating of transition metal macrocycles, such as Fe–phthalocyanine and Fe–porphyrin in the original research by Jasinski and Yeager and co-workers.[10−13] Subsequently, the pyrolysis of these expensive macrocycles was improved by pyrolyzing more common and cost-effective precursors that comprised of N-rich substances, transition metal salts, and carbon supports.[14−18] Thus far, the state-of-the-art NPMCs exhibit much higher ORR activity and durability than those of Pt-based catalysts in alkaline electrolytes.[19] However, the

Received: May 17, 2014
Revised: September 7, 2014
Published: September 23, 2014

performances of NPMCs in acidic media, which, in such media, the PEMFCs are practically operated, still require improvement.[7,20,21] Thus, the development of efficient and durable NPMCs for ORR in acidic media has practical significance.[22,23] Although the exact nature and precise active sites of NPMCs for ORR are still not very clear, both quantum chemical calculations[24,25] and experimental reports[17,23,26] have revealed that nitrogen and/or Fe−N_x moieties play an essential role in catalyzing the ORR. It should be noted that the activity and durability of transition-metal-based NPMCs greatly depend upon the selection of precursors and the heat treatment process.

The graphitic carbon nitride (g-C_3N_4) polymer,[27−29] with a graphite-like structure, is an effective catalyst in the fields of photochemical splitting of water[30,31] and heterogeneous catalysis in various organic systems[32,33] because of its peculiar thermal stability, appropriate electronic structure, and low-cost preparation.[34−36] In particular, g-C_3N_4 contains alleged "nitrogen pots" with six nitrogen lone-pair electrons, which are ideal sites for metal inclusion.[32,37] Furthermore, g-C_3N_4 can also be used as a dopant to incorporate N atoms into carbon substrate through heat treating.[38] Accordingly, g-C_3N_4 with a high N content can be chosen as a perfect N source to coordinate with Fe ions, forming and incorporating potential ORR active sites into carbon support during the pyrolysis process. Recently, Byon et al.[39] synthesized a Fe−N−C catalyst by pyrolyzing a mixture of Fe salt, g-C_3N_4 (N source), and graphene at 800 °C. The ORR mass activity was only 1.5 mA mg^{-1} at 0.75 V [versus reversible hydrogen electrode (RHE)], but it is almost one of the best Fe−N−C catalysts with g-C_3N_4 as the N source in the acid fuel cell. Up to now, there are rare reports on NPMCs that use g-C_3N_4 as the N source and carbon black as the support with competitive ORR performance to Pt in acidic medium.

Herein, we prepared a novel g-C_3N_4-derived NPMC with high ORR activity and stability in acidic medium, by *in situ* polymerizing Fe-doped graphitic carbon nitride on carbon black (Fe−g-C_3N_4@C). During the pyrolysis process, Fe−g-C_3N_4 was decomposed and, thereby, Fe−N moieties were introduced into the carbon substrate. Furthermore, our synthetic strategy for the NPMCs had a multitude of advantages. First of all, Ketjenblack EC 600JD (KJ-600) was chosen as the carbon support because of its excellent properties, including good electrical conductivity, high Brunauer−Emmett−Teller (BET) surface area of ∼1400 m^2 g^{-1}, and good corrosion resistance,[40] which are beneficial to improve the ORR activity and stability. Second, the *in situ* condensation of Fe−g-C_3N_4 on carbon black is through a simple pyrolysis step without using a cryogenic instrument, while the polymerization of polyaniline,[16,18,41] which is commonly reported as a N source, needs to be synthesized with constant stirring below 10 °C for about 1 day. Finally, the resulting catalyst does not need post-treatment, including acid leaching and a second heat treatment, which drastically shortens the time required for sample preparation. In this work, the influences of the pyrolysis temperature and Fe content on the ORR performance of the catalysts were investigated. Meanwhile, the possible ORR active sites were also explored.

2. EXPERIMENTAL SECTION

2.1. Reagents and Materials. Ketjenblack EC 600JD (KJ-600) was purchased from AkzoNobel, and dicyandiamide (DCD) was bought from Aladdin. Commercial 20 wt % Pt/C catalyst and 5 wt % Nafion solution were purchased from Alfa Aesar. Other chemicals, such as $HClO_4$, HCl, $FeCl_3·6H_2O$, and ethanol, were bought from China Medicine Shanghai Chemical Reagent Corp. All reagents were analytically pure and used as received without further purification. All aqueous solutions were prepared using deionized water with a resistivity of 18.2 MΩ cm provided by a Millipore Milli-Q Lab apparatus (Nihon Millipore, Ltd.)

2.2. Synthesis of Fe−g-C_3N_4@C and Pyrolyzed Fe−N−C Composite. Carbon support KJ-600 was treated in HCl solution for 12 h to remove any metal impurities first.[18] In a typical preparation, 1 g of DCD was dissolved in 20 mL of deionized water with stirring at 80 °C. Then, different amounts of $FeCl_3·6H_2O$ (0.05, 0.1, and 0.15 g) were added to form iron complexes. The mass ratio of Fe salt/DCD is 5, 10, and 15% in the precursor, and then the corresponding products were denoted as 5% Fe−g-C_3N_4@C, 10% Fe−g-C_3N_4@C, and 15% Fe−g-C_3N_4@C or pyrolyzed 5% Fe−N−C, 10% Fe−N−C, and 15% Fe−N−C, respectively. Subsequently, 0.1 g of pretreated carbon black was added to the solution. The mixture was then continually stirred at 120 °C until the solution completely evaporated. The resulting solid mixture was then collected and ground with a mortar and pestle for 15 min. Finally, the as-received powder was calcined in two consecutive steps: (1) the solid products were first heated to 550 °C at a rate of 10 °C/min and tempered at this temperature for another 3 h under argon flow to form the complex of Fe−g-C_3N_4@C, and (2) as-received Fe−g-C_3N_4@C was subsequently heated to a higher temperature (e.g., 700, 750, 800, or 900 °C) at a rate of 10 °C/min and maintained for 1 h to obtain pyrolyzed Fe−g-C_3N_4@C, denoted as Fe−N−C composite as well. For references, g-C_3N_4 and Fe−g-C_3N_4 were prepared by the same procedure as Fe−g-C_3N_4@C with the precursors of DCD and DCD/$FeCl_3·6H_2O$, respectively. Owing to the loss of intermediate gas species mainly decomposed from g-C_3N_4, the crude final product of the Fe−N−C composite is about 0.2 ± 0.05 g after the pyrolysis process.

2.3. Material Characterization. X-ray diffraction (XRD) spectra were recorded on a Rigaku SmartLab 3 kW diffractometer with Cu Kα radiation (λ = 0.154 05 nm), and the scanning rate was 4°/min. Fourier transform infrared spectroscopy (FTIR) was performed on a Nicolet 470 FTIR spectrophotometer as KBr pellets in the 4000−400 cm^{-1} region. X-ray photoelectron spectroscopy (XPS) data were obtained on a PHI Quantum 2000 scanning ESCA microprobe (Physical Electronics) operated at 15 kV, 25 W, and 1486.6 eV with monochromated Al Kα radiation, and binding energies were corrected with reference to the C 1s peak at 284.8 eV. The transmission electron microscopy (TEM) and high-resolution transmission electron microscopy (HRTEM) images were taken on JEM-2100 at 200 kV. The statistical analysis of the metal particle cross-sectional diameter was performed using the ImageJ program. Thermogravimetric analysis (TGA) of the catalysts was conducted using a Shimadzu DTG-60H thermal analyzer, and samples were heated from ambient temperature to 900 °C at a rate of 10 °C min^{-1} in flowing N_2.

2.4. Preparation of the Working Electrodes. A rotating disk electrode (RDE, disk area of 0.196 cm^2) and a rotating ring-disk electrode (RRDE, disk area of 0.247 cm^2) were used as working electrodes to characterize the ORR activity and electron selectivity of the catalysts, respectively. Prior to the electrochemical test, the RDE and RRDE were polished with 1.0 μm alumina slurry and then with 0.3 μm slurry to afford a

dx.doi.org/10.1021/cs500673k | ACS Catal. 2014, 4, 3928−3936

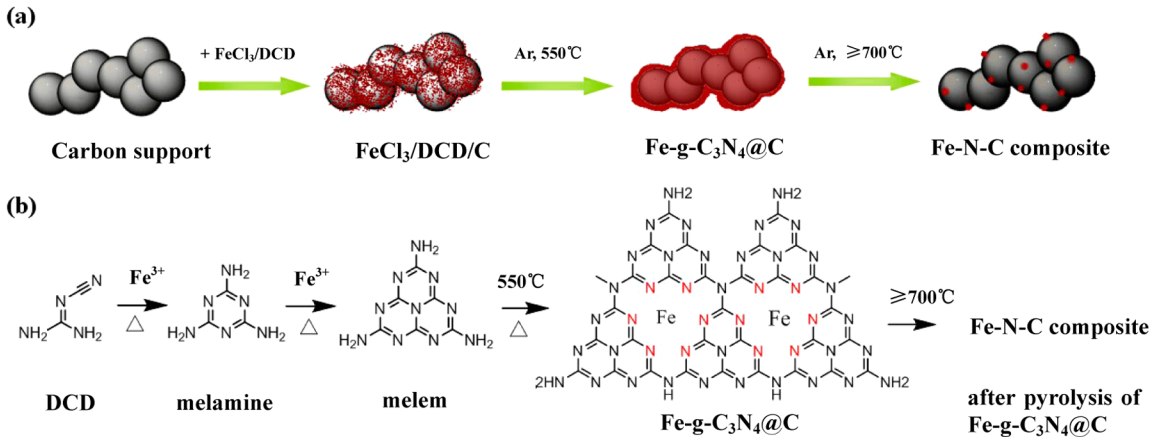

Figure 1. (a) Schematic synthetic strategy and (b) proposed formation mechanism of the Fe−N−C composite after pyrolysis of Fe−g-C_3N_4@C.

mirror finish. The catalyst ink was prepared by ultrasonically mixing 6 mg of pyrolyzed Fe−N−C composite with 500 μL of ethanol, 450 μL of deionized water, and 50 μL of 5 wt % Nafion for 1 h. Then, the suspension of pyrolyzed Fe−N−C composite was loaded onto the glassy-carbon disk surface of RDE (20 μL) and RRDE (25 μL), resulting in a catalyst loading of 0.6 mg cm^{-2}. For comparison, a 1 mg mL^{-1} suspension of commercial 20 wt % Pt/C (JM) was obtained according to the same procedure described above, and the catalyst loading is 20 μg_{Pt} cm^{-2}.

2.5. Electrocatalytic Measurements. All electrochemical measurements were carried out in a standard three-electrode cell working with a CHI electrochemical station (model 760d). Graphite rod was used as counter electrode to avoid any potential contamination of a NPMC by platinum. RHE was used as a reference electrode, and all potentials in this work are referred to RHE.

In RDE tests, cyclic voltammetry (CV) characterization of pyrolyzed Fe−N−C composite was carried out in O_2-saturated 0.1 M $HClO_4$ electrolyte in the potential range from 0.2 to 1.0 V at a scan rate of 10 mV s^{-1} and the electrode rotation speed is 900 rpm. To correct the background current, the voltammogram recorded in N_2-saturated 0.1 M $HClO_4$ was subtracted from the voltammogram recorded in O_2-saturated electrolyte. In RRDE experiments, the ring potential was set to 1.2 V. All of the current densities in this work were normalized in reference to the geometric area of RDE (0.196 cm^2) or RRDE (0.247 cm^2).

The accelerated durability tests (ADTs)[42] of the pyrolyzed Fe−N−C composite were performed in N_2-saturated 0.1 M $HClO_4$ in the potential range from 0.6 to 1.0 V with a scan rate of 50 mV s^{-1}. The corresponding Pt/C data were recorded in 0.1 M $HClO_4$ solution with the same test conditions as that of pyrolyzed Fe−N−C composite.

The current density (J_k) of the pyrolyzed Fe−N−C composite was calculated on the basis of the Koutecky−Levich equations (eqs 1−3)[43]

$$\frac{1}{J} = \frac{1}{J_L} + \frac{1}{J_K} = \frac{1}{B\omega^{1/2}} + \frac{1}{J_K} \quad (1)$$

$$B = 0.62nFC_0(D_0)^{2/3}\nu^{-1/6} \quad (2)$$

$$J_k = nFkC_0 \quad (3)$$

where J is the measured current density, J_K and J_L are the kinetic- and diffusion-limiting current densities, respectively, ω is the angular velocity of the disk ($\omega = 2\pi N$, where N is the linear rotation speed), n is the overall number of electrons transferred in the oxygen reduction, F is the Faraday constant (96 485 C mol^{-1}), C_0 is the bulk concentration of O_2, ν is the kinematic viscosity of the electrolyte, and k is the electron transfer rate constant.

The hydrogen peroxide yield (H_2O_2, %) and the number of electrons transferred (n) in the ORR are estimated from eqs 4 and 5, respectively[39]

$$H_2O_2\ (\%) = \frac{2I_R}{(N|I_D|) + I_R} \times 100 \quad (4)$$

$$n = 4 - \left(2\frac{H_2O_2\ (\%)}{100}\right) \quad (5)$$

where N = 0.37 is the collection efficiency, I_D is the disk current, and I_R is the ring current.

3. RESULTS AND DISCUSSION

3.1. Preparation and Physical Characterization of Fe−g-C_3N_4@C and Pyrolyzed Fe−N−C Composite. The synthetic process of the pyrolyzed Fe−N−C composite is illustrated schematically in Figure 1a. The first step was to mix the three precursors, including carbon black Ketjenblack EC 600JD, DCD, and iron salt (denoted as $FeCl_3$/DCD/C), in deionized water (see the Experimental Section for details). The mixed solution was then heated to 120 °C with continuous stirring to evaporate to dryness. In the second step, the resultant solid mixture was annealed at 550 °C under argon flow for 3 h to trigger the *in situ* polymerization of DCD with Fe ions on carbon black, resulting in a composite of Fe−g-C_3N_4@C.[32] Subsequently, the further heat treatment of Fe−g-C_3N_4@C above 700 °C gave rise to the decomposition of Fe−g-C_3N_4, thereby generating ORR active sites. The proposed reaction mechanism of the formation of the pyrolyzed Fe−N−C composite is shown in Figure 1b.

The polymerization and decomposition of Fe−g-C_3N_4@C as well as the formation of ORR active sites were also investigated by thermogravimetry (TG), FTIR, and XRD. As show in Figure S1 of the Supporting Information, the thermal polymerization of Fe−g-C_3N_4@C is between 400 and 550 °C, while a whole mass of $FeCl_3$/DCD/C is abruptly lost from 550 to 600 °C, owing to the decomposition of Fe−g-C_3N_4. Panels a and b of

dx.doi.org/10.1021/cs500673k | ACS Catal. 2014, 4, 3928−3936

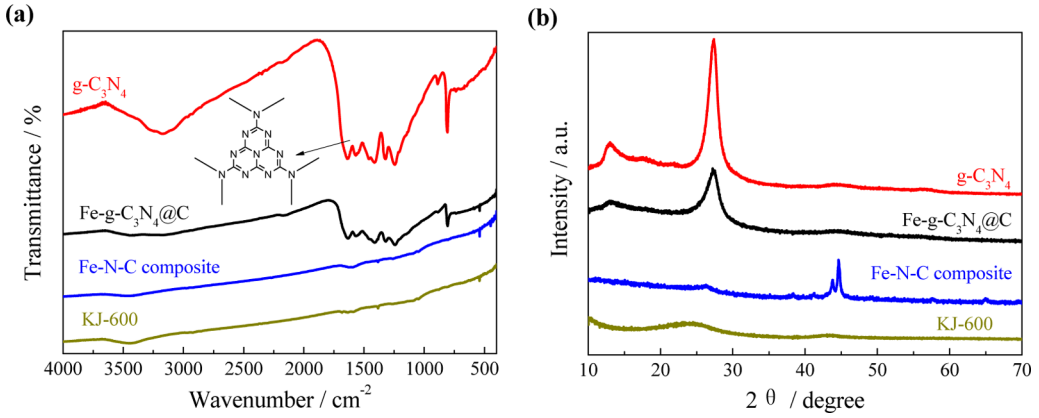

Figure 2. (a) FTIR spectra and (b) XRD patterns of g-C_3N_4, Fe−g-C_3N_4@C, pyrolyzed Fe−N−C composite, and KJ-600 (inset of panel a shows the molecular structure of heptazine-derived repeating units).

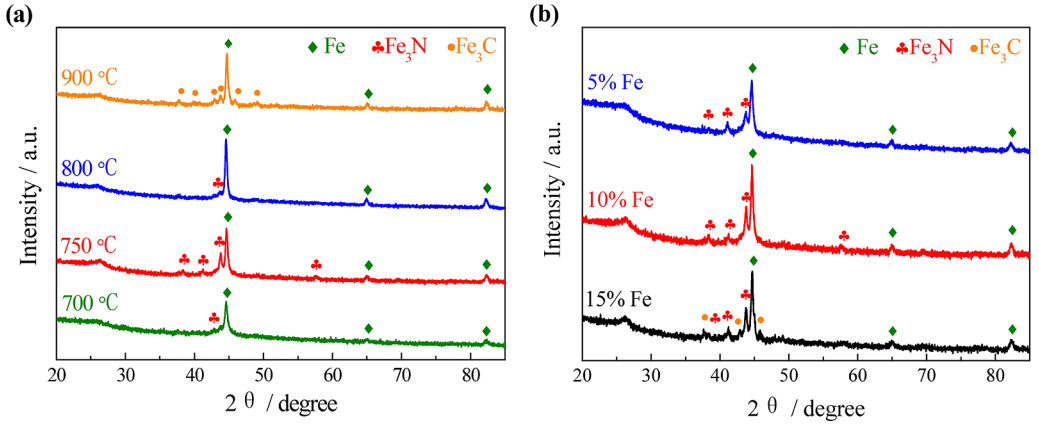

Figure 3. XRD patterns of (a) pyrolyzed 10% Fe−N−C composites synthesized at different temperatures and (b) pyrolyzed Fe−N−C composites with different Fe contents synthesized at 750 °C.

Figure 2 show the infrared (IR) and XRD spectra of g-C_3N_4, Fe−g-C_3N_4@C, pyrolyzed Fe−N−C composite, and KJ-600. The intense bands at 1639.5, 1570.1, 1460.2, and 1411.9 cm^{-1} (see the g-C_3N_4 spectrum in Figure 2a) are assigned to typical stretching vibration modes of heptazine-derived repeating units (see the inset structure).[44] The intense band at 808.2 cm^{-1} represents the out-of-plane bending vibration characteristic of heptazine rings.[44] The bands at 1321.3 and 1246.1 cm^{-1} correspond to the stretching vibration of connected units of C−N(−C)−C (full condensation) or C−NH−C (partial condensation).[44] The XRD spectrum of g-C_3N_4 (Figure 2b) reveals a typical graphite-like structure. The strong peak at 27.4° is indicative of the layered stacking with a distance of 0.326 nm, which is consistent with the reported result,[36] and the in-planar repeating unit with a period of 0.682 nm is clearly shown by the XRD peak at 12.98°. After the inclusion of the Fe ion and carbon support, both the XRD and IR patterns suffer from a significant intensity decrease, which indicates that the inclusion of the Fe ion and/or carbon support can result in an inhibition of polymeric condensation,[32] while it is interesting to observe that, in the XRD pattern of Fe−g-C_3N_4@C, no peaks originating from iron species (such as iron, iron oxides, iron nitrides, iron chlorides, and iron carbides) are found, which manifests that the iron species are chemically coordinated to the g-C_3N_4 host, most likely in the form of Fe−N bonds.[37] When Fe−g-C_3N_4@C was pyrolyzed above 700 °C, the aromatic C−N and C═N stretching modes in the range of 1100−1650 cm^{-1} disappear (blue in Figure 2a), while XRD peaks attributed to Fe species (blue in Figure 2b) illustrate that, when above 700 °C, Fe−g-C_3N_4 is decomposed and may be prone to transform to a preferred configuration, including the ORR active sites.

To further study the morphology and structure of pyrolyzed Fe−N−C composite, XRD, HRTEM, and XPS were carried out. Figure 3a shows the XRD patterns of the pyrolyzed Fe−N−C composite synthesized at different temperatures with the same Fe content of 10%. The broad and relatively weak peak at 25.9° corresponding to the (002) carbon plane indicates the low graphitization degree. Each of the heat-treated samples gives a set of peaks at 44.6°, 64.9°, and 82.3°, which are attributed to metallic iron [Joint Committee on Powder Diffraction Standards (JCPDS) number 65-4899]. It is noteworthy that the XRD pattern of the pyrolyzed Fe−N−C composite (750 °C) shows an apparent peak at 43.7°, which is significantly different from other samples. This peak is attributed to the characteristic peak of Fe_3N (JCPDS number 49-1664). When the pyrolysis temperature rises to 900 °C, Fe_3C (JCPDS number 65−2412) is detected. In Figure 3b, all of the samples pyrolyzed at 750 °C with different Fe contents show the peaks of Fe_3N, which indicates that Fe_3N may tends to form at 750 °C. When the Fe content is reduced to 5%, the peak intensity of Fe_3N becomes weaker, indicating the lower crystallinity of Fe_3N. When the Fe content was increased to 15%, the peaks of Fe_3C come into being. Comprehensively,

dx.doi.org/10.1021/cs500673k | ACS Catal. 2014, 4, 3928−3936

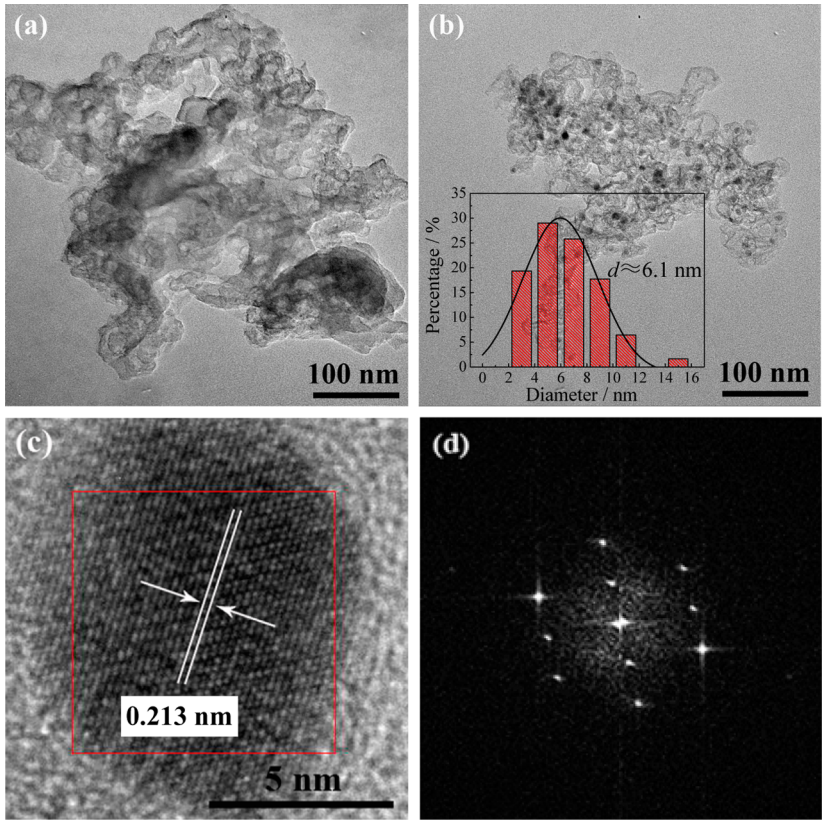

Figure 4. (a) TEM image of Fe−g-C_3N_4@C. (b) TEM image of the pyrolyzed 10% Fe−N−C (750 °C) composite (inset shows the metal particle size distribution). (c) HRTEM image of a metal particle in panel b. (d) Corresponding SAED pattern of the metal nanoparticle.

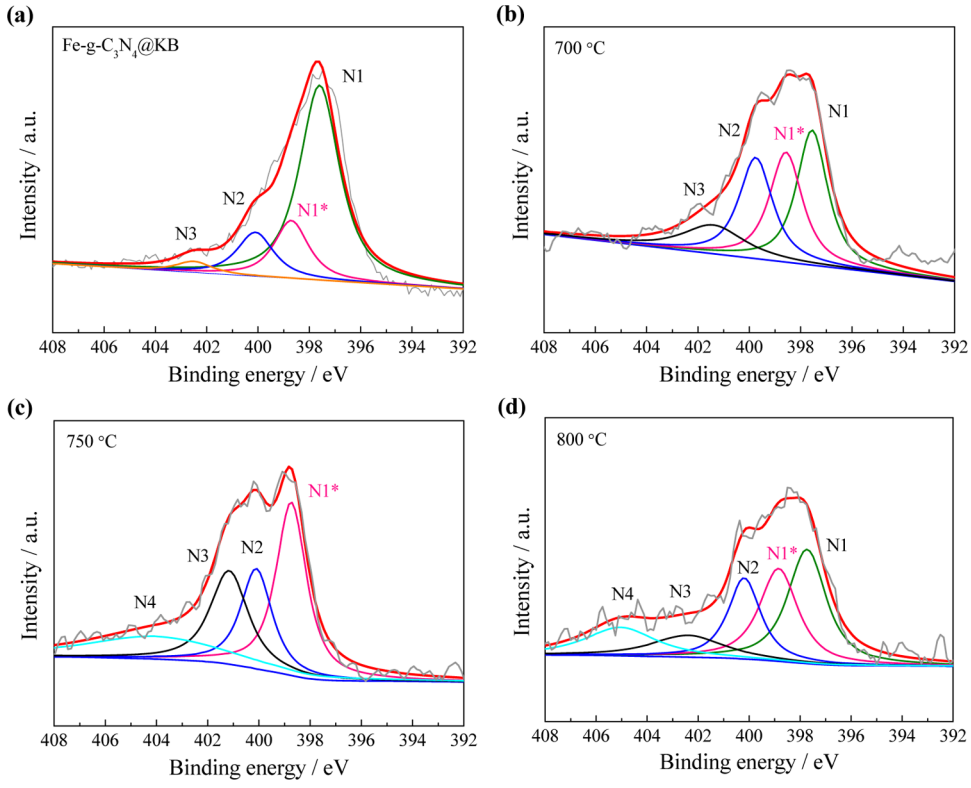

Figure 5. High-resolution XPS spectra of N 1s at (a) Fe−g-C_3N_4@C and (b−d) pyrolyzed 10% Fe−N−C composites synthesized at different temperatures.

dx.doi.org/10.1021/cs500673k | ACS Catal. 2014, 4, 3928−3936

Table 1. Percentage Content of Different N Species in Total N Amount for Fe−g-C_3N_4@C and Pyrolyzed Fe−N−C Composites, Calculated from the N 1s Data of Figure 5

	N1 pyridinic N (%)	N1* Fe−N_x (%)	N2 pyrrolic N (%)	N3 quaternary N (%)	N4 oxidized N (%)
Fe−g-C_3N_4@C	67.6	13.4	15.1	3.9	
700 °C	32.3	27.8	26.2	13.7	
750 °C		37.3	21.3	21.7	20.7
800 °C	30.6	24.8	18.9	11.1	14.6

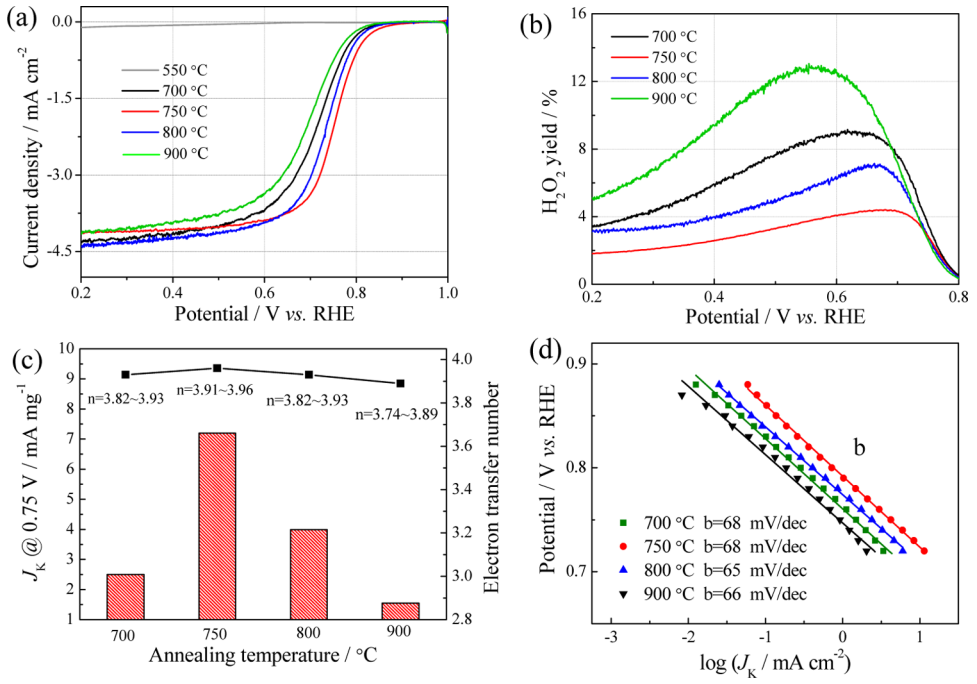

Figure 6. (a) ORR activity of Fe−g-C_3N_4@C and pyrolyzed Fe−N−C composite. (b) H_2O_2 yield of the pyrolyzed Fe−N−C composite, in O_2-saturated 0.1 M $HClO_4$ at 900 rpm, with a scan rate of 10 mV s^{-1}. The Pt ring electrode was polarized at 1.2 V, and the catalyst loading is 0.6 mg cm^{-2}_{geo}. (c) Electron transfer number at 0.4 V and the kinetic-limiting current density (J_K) at 0.75 V for the pyrolyzed Fe−N−C composite. (d) Tafel ORR plots for the pyrolyzed Fe−N−C composite.

considering these results, it can be conclude that there is competition between the formation of Fe_3C and Fe_3N. In our work, pyrolyzing at 750 °C with 10% content of Fe is the optimum condition to form Fe_3N.

Figure 4a shows the TEM of Fe−g-C_3N_4@C, in which Fe−g-C_3N_4 is loaded on carbon black homogeneously and no detectable metal nanoparticles are found, which again confirms that Fe ions are doped in g-C_3N_4 structures rather than the formation of iron or iron oxide particles. In contrast, for pyrolyzed Fe−N−C composite synthesized at 750 °C with a Fe content of 10% [denoted as 10% Fe−N−C (750 °C)], as seen in Figure 4b, the crystalline metal nanoparticles with an average particle diameter of 6.1 nm (inset) are uniformly dispersed on the carbon black. The XPS broad scan (in Figure S2 of the Supporting Information) shows the existence of C, N, O, and Fe in Fe−g-C_3N_3@C and pyrolyzed Fe−N−C composites. In comparison to Fe−g-C_3N_3@C, the pyrolyzed Fe−N−C composite shows a serious decline in the total N amount because of the decomposition of g-C_3N_4; nevertheless, the pyrolyzed Fe−N−C composite shows a relatively high N content of 6.5 atomic % (see Table S1 of the Supporting Information). The iron nanoparticle wrapped in carbon is further corroborated by the HRTEM (Figure 4c). It can be measured that the lattice spacing is about 0.213 ± 0.006 nm, which is slightly larger than the standard value of 0.204 nm, corresponding to the [110] plane of metallic Fe. The larger lattice space might be ascribed to the spaces of iron with intercalated nitrogen atom, which accordingly enlarges the lattice constant.[43] The SAED pattern (in Figure 4d) of the nanoparticle reveals that the nanoparticles are single crystal. Furthermore, increasing the Fe content to 15% could result in the agglomeration of 5−80 nm Fe nanoparticles, while few nanoparticles are visible in the pyrolyzed Fe−N−C composite with a Fe content of 5% (Figure S3a of the Supporting Information).

XPS analysis was used to explore the effects of pyrolysis on the state of the catalyst surface. A comparison of N 1s spectra of Fe−g-C_3N_4@C and pyrolyzed Fe−N−C composite synthesized at different temperatures is shown in Figure 5. The peaks in N 1s spectra of all samples (panels a−d of Figure 5) are divided into four N species: pyridinic N (N1 and N1*, 397−399 eV),[45] pyrrolic N (N2, 400 ± 0.3 eV),[16] quaternary N (N3, 401−403 eV),[46] and oxidized N (N4, 404−405 eV), in which pyridinic N (397−399 eV) can coordinate with Fe in the form of Fe−N_x.[39,46] In this work, N1 (at 397.6 eV) is ascribed to the nitrogen−carbon support interaction,[46] N1* (398.6 ± 0.3 eV) can be regarded as N that bonds to metal (Fe−N_x),[37,39,43] while oxidized N species do not significantly contribute to the ORR

dx.doi.org/10.1021/cs500673k | ACS Catal. 2014, 4, 3928−3936

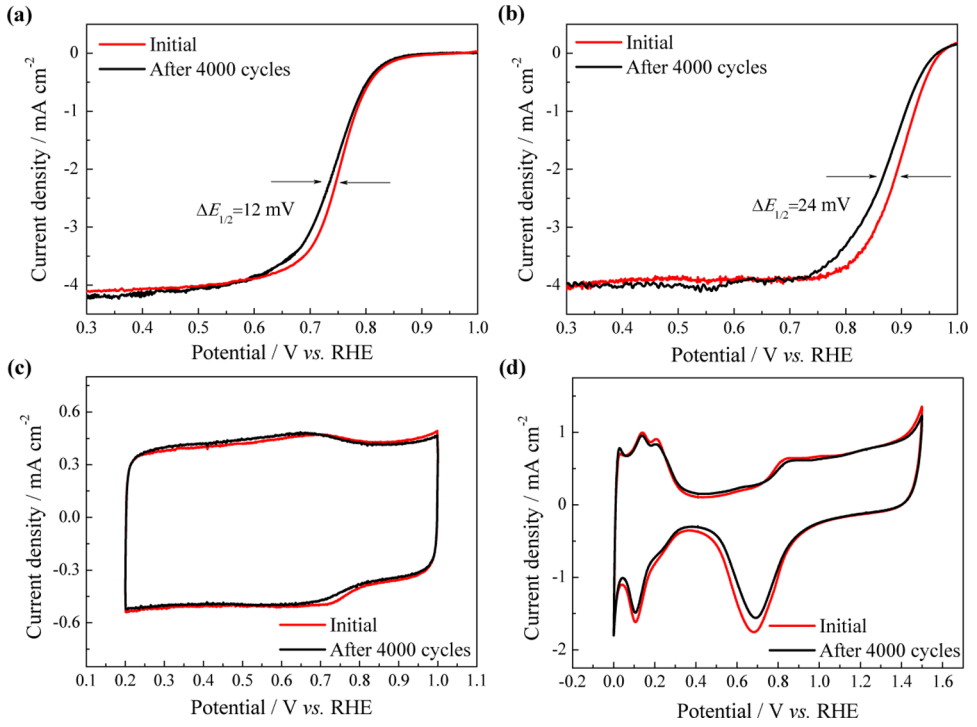

Figure 7. ORR activity of (a) pyrolyzed 10% Fe−N−C (750 °C) composite and (b) Pt/C (20 μg_{Pt} cm^{-2}). CV curves of (c) pyrolyzed 10% Fe−N−C (750 °C) composite and (d) Pt/C before and after the ADT. The potential cycles were from 0.6 to 1.0 V in a N_2-saturated 0.1 M $HClO_4$ solution with a scan rate of 50 mV s^{-1}.

performance and are unstable under fuel cell operating conditions.[43] The percentage contents of different types of N in total N amount were calculated (in Table 1). In comparison of the ratio of N species in all catalyst samples, it can be conclude that N1 is dominated in Fe−g-C_3N_4@C, and for pyrolyzed samples, the percentage content of N1* (Fe−N_x, most likely in the form of Fe_3N) increased to a maximum value at the temperature of 750 °C, which is consistent with the XRD result. Additionally, the quaternary N also reaches a maximum at 750 °C.

Moreover, the XPS spectra in Fe 2p regions for Fe−g-C_3N_4@C and pyrolyzed samples are also demonstrated in Figure S4 of the Supporting Information. The metallic Fe and Fe^{II} are dominant in the Fe−g-C_3N_4@C sample. However, Fe^{III} can be detected in all pyrolyzed Fe−N−C composites, and the content of Fe^{III} reaches a maximum at 750 °C, as shown in Figure S4 of the Supporting Information. These Fe^{III} species can be attributed to Fe^{III}−N_x and Fe^{III} carbide.[47] It should be noted that the binding energy of 711.1 ± 0.2 eV of the Fe^{III} peak is close to the value of 711.7 eV measured for iron(III) porphyrin.[48] In combination with the XRD results and N 1s XPS spectra discussed above, it can be concluded that Fe^{III} may bond to pyridinic N (N1*, 397−399 eV) to form Fe−N_x species and the optimum temperature for the formation of this structure is 750 °C.

3.2. ORR Performance of Fe−g-C_3N_4@C and Pyrolyzed Fe−N−C Composite. The ORR activity for Fe−g-C_3N_4@C and pyrolyzed samples synthesized at different temperatures in 0.1 M $HClO_4$ is shown in Figure 6a. Obviously, Fe−g-C_3N_4@C exhibits negligible ORR activity, presumably because the active sites for ORR had not been formed before the pyrolysis process. In addition, the small specific surface area (typically 10 m^2 g^{-1})[36] and poor conductivity[49] of g-C_3N_4 loaded on the surface of carbon black may impede the mass transfer and transport of electrons, while pyrolysis leads to a significant improvement in activity and less H_2O_2 yield, which are due to the decomposition of Fe−g-C_3N_4@C and abundant defect sites exposed on the surface of carbon black. Furthermore, the annealing temperature has great influence on the catalytic activity. With ramping the heat treatment temperature from 700 to 900 °C, the ORR kinetic currents first increase to a maximum at 750 °C with a half-wave potential of 0.75 V and then decrease with a further increase of the temperature. Furthermore, the pyrolyzed Fe−N−C composite (750 °C) shows the lowest H_2O_2 yield of 2.6% at 0.4 V.

Figure 6c displays the electron transfer number (n) at 0.4 V and the ORR mass activity (J_K) at 0.75 V of pyrolyzed Fe−N−C composites synthesized at different temperatures. It is clear that pyrolyzed Fe−N−C composite (750 °C) displays the optimal activity with the highest electron transfer of 3.95 at 0.4 V and the highest mass activity of 7.2 mA mg^{-1} at 0.75 V, which is much higher than the reported value of NPMCs synthesized from g-C_3N_4-based precursors in acid (~1.5 mA mg^{-1} at 0.75 V).[39]

The Tafel slope was also determined to evaluate the ORR kinetic character of pyrolyzed Fe−N−C composites (Figure 6d). The Tafel plots of Fe−N−C composites pyrolyzed at different temperatures show two distinct slope regions. In comparison to the well-established "dual" Tafel slope for the ORR on Pt (60 and 120 mV dec^{-1} at potential higher and lower than 0.8 V, respectively).[50,51] The Tafel slope values of 65−68 mV dec^{-1} observed with the pyrolyzed Fe−N−C composites at high potentials suggest that the ORR rate on pyrolyzed Fe−N−C composites may be determined by migration of adsorbed oxygen intermediates.[52] The difference in Tafel slope values for pyrolyzed Fe−N−C composites and Pt implies a different nature of the ORR active sites in these two catalysts.

dx.doi.org/10.1021/cs500673k | ACS Catal. 2014, 4, 3928−3936

Furthermore, the content of the metal plays an important role in achieving high catalytic activity.[16] Consequently, the mass ratio of Fe salt/DCD in the initial mixture was changed from 5 to 15%, following the synthesis procedure described in section 2.1. Figure S5a of the Supporting Information shows the polarization curves of pyrolyzed Fe−N−C composites with different Fe contents. Moreover, Figure S5b of the Supporting Information displays electrochemical activity given as the kinetic-limiting current density (J_K) at 0.75 V and the ORR selectivity given as the electron transfer number of pyrolyzed Fe−N−C composites with different Fe contents. As shown in panels a and b of Figure S5 of the Supporting Information, pyrolyzed 10% Fe−N−C shows the optimal ORR activity and selectivity.

In conclusion, with the Fe salt/DCD mass ratio of 1:10 and the pyrolyzed temperature at 750 °C, the pyrolyzed Fe−N−C composite shows the optimum ORR activity. This is because the activity of the Fe−N−C catalyst is much related with the concentration of the active site that existed as FeN_x or CN species. When the value of Fe salt/DCD is lower than 10%, for instance, 5%, increasing the Fe content may lead to an increase in the amount of active sites until all pyridinic N is coordinated with Fe. Then, increasing the Fe content (to 15%) may produce extra uncoordinated metal, which leads to the size increase and aggregation of nanoparticles (as shown in Figure S3b of the Supporting Information).

In combination with the XRD and XPS results of pyrolyzed Fe−N−C composites discussed above, we draw the following conclusions: (1) The ORR active sites are closely related to Fe_3N, while the forming of Fe_3C will inhibit the ORR. (2) Both pyridinic N (which may bond to Fe^{III} to form Fe_3N) and quaternary N in the pyrolyzed Fe−N−C composites are conducive to catalyze the ORR and can serve as catalytically active sites for oxygen reduction. A similar relationship between the content of these two types of nitrogen and ORR activity was also reported in other literature.[17,46]

However, up to now, the exact nature of the active site(s) in these NPMC catalysts synthesized using a heat treatment approach remains controversial. Some researchers have proposed that $M-N_x$ species are the active sites for ORR.[16,53,54] On the contrary, others have proposed that transition metals are not part of the active sites but play a role as catalysts to incorporate stable N-containing sites on the carbon substrate.[26,55,56]

3.3. ORR Durability Characterization. The electrochemical durability in corrosive acidic media is also an important issue in evaluating the performance of the catalyst. The durability of pyrolyzed 10% Fe−N−C (750 °C) composite and 20 wt % Pt/C in acid was determined by comparing the changes for ORR activity before and after the ADTs.[42] The samples were continuously cycled from 0.6 to 1.0 V with a scan rate of 50 mV s^{-1} in nitrogen-saturated 0.1 M $HClO_4$ for 4000 cycles. The ORR activities of pyrolyzed 10% Fe−N−C (750 °C) and Pt/C (20 μg_{Pt} cm^{-2}) before and after 4000 cycles were shown in panels a and b of Figure 7, respectively. There is only a 12 mV shift of the half-wave potential ($\Delta E_{1/2}$) for the pyrolyzed 10% Fe−N−C (750 °C) composite. In comparison, the shift of $\Delta E_{1/2}$ is 24 mV for commercial Pt/C during ADTs. The results suggest that the pyrolyzed 10% Fe−N−C (750 °C) composite exhibits much better durability than commercial Pt/C under the same test conditions. This may be because the possible activity site for this type of Fe−N−C catalyst could not be easy to reduce as a result of the protection of N-doped carbon KJ-600 formed during the pyrolysis process. Additionally, TEM results of Figure 4 and Figure S3 of the Supporting Information also confirm that the Fe nanoparticle was wrapped by carbon, which may protect the metal from dissolving. A similar result that the wrapped Fe nanoparticle could not dissolve in acid was observed in a previous report as well.[57]

The CV curves of the pyrolyzed 10% Fe−N−C (750 °C) composite and Pt/C are shown in panels c and d of Figure 7, respectively. The decay of the intensity of Fe^{II}/Fe^{III} redox peaks at ca. 0.65 V may be a manifestation dissolution of Fe species, including some unstable active sites. However, Pt/C suffers from greater degradation during the ADT, as shown in Figure 7d. This is because Pt is likely to dissolve in electrolyte, aggregate into larger particles, and detach from the support, resulting in poor durability in acidic medium.[58] Consequently, the pyrolyzed 10% Fe−N−C (750 °C) composite is more stable than Pt/C, which may be because of the more stable quaternary nitrogen, which is regarded as another active site for ORR.

4. CONCLUSION

In summary, we reported a facile and scalable method to prepare a novel NPMC for ORR by pyrolyzing the complex of Fe−g-C_3N_4@C at different temperatures. The RDE/RRDE tests demonstrate that the pyrolyzed 10% Fe−N−C (750 °C) composite exhibits excellent ORR activity, almost four electron transfer processes, and better durability in comparison to Pt/C in acid electrolyte, which indicate that the pyrolyzed 10% Fe−N−C (750 °C) material can be a promising non-precious metal cathode catalyst for fuel cells. Comprehensively, analyzing the XRD, XPS, and RDE/RRDE results, we surmise that both Fe_3N (where Fe ions probably bonded with pyridinic nitrogen) and quaternary nitrogen incorporated into the carbon matrix are the possible ORR active sites in the pyrolyzed Fe−N−C catalysts.

■ ASSOCIATED CONTENT

Supporting Information

Additional characterization data, including TGA of Fe−g-C_3N_4@C and the mixed precursor (Figure S1), XPS spectra of 10% Fe−g-C_3N_4@C and pyrolyzed 10% Fe−N−C (750 °C) composite (Figure S2), content of Fe, N, C, and O elements in 10% Fe−g-C_3N_4@C and pyrolyzed 10% Fe−N−C (750 °C) composite (Table S1), TEM images of pyrolyzed Fe−N−C composites with different Fe contents (Figure S3), broad and high-resolution XPS spectra of Fe 2p at Fe−g-C_3N_4@C and pyrolyzed Fe−N−C composites (Figure S4), and ORR activity and H_2O_2 yield of pyrolyzed Fe−N−C composites with different Fe contents (Figure S5). This material is available free of charge via the Internet at http://pubs.acs.org/.

■ AUTHOR INFORMATION

Corresponding Authors

*E-mail: yangwh@hqu.edu.cn.

*E-mail: sgsun@xmu.edu.cn.

Notes

The authors declare no competing financial interest.

■ ACKNOWLEDGMENTS

This work was financially supported by the National Natural Science Foundation of China (21473063, 21103055, and 21321062).

REFERENCES

(1) Yu, X.; Ye, S. *J. Power Sources* **2007**, *172*, 145−154.
(2) Wang, B. *J. Power Sources* **2005**, *152*, 1−15.
(3) Yang, W. H.; Wang, H. H.; Chen, D. H.; Zhou, Z. Y.; Sun, S. G. *Phys. Chem. Chem. Phys.* **2012**, *14*, 16424−16432.
(4) Li, Y.; Li, Y.; Zhu, E.; McLouth, T.; Chiu, C. Y.; Huang, X.; Huang, Y. *J. Am. Chem. Soc.* **2012**, *134*, 12326−12329.
(5) Di Noto, V.; Negro, E.; Vezzù, K.; Toniolo, L.; Pace, G. *Electrochim. Acta* **2011**, *57*, 257−269.
(6) Stephens, I. E.; Bondarenko, A. S.; Grønbjerg, U.; Rossmeisl, J.; Chorkendorff, I. *Energy Environ. Sci.* **2012**, *5*, 6744−6762.
(7) Wu, G.; Zelenay, P. *Acc. Chem. Res.* **2013**, *46*, 1878−1889.
(8) Jaouen, F.; Proietti, E.; Lefevre, M.; Chenitz, R.; Dodelet, J. P.; Wu, G.; Chung, H. T.; Johnston, C. M.; Zelenay, P. *Energy Environ. Sci.* **2011**, *4*, 114−130.
(9) Chen, Z.; Higgins, D.; Yu, A.; Zhang, L.; Zhang, J. *Energy Environ. Sci.* **2011**, *4*, 3167−3192.
(10) Jasinski, R. *Nature* **1964**, *201*, 1212−1213.
(11) Badger, G.; Jones, R. A.; Laslett, R. *Aust. J. Chem.* **1964**, *17*, 1028−1035.
(12) Jasinski, R. *J. Electrochem. Soc.* **1965**, *112*, 526−528.
(13) Gupta, S.; Tryk, D.; Bae, I.; Aldred, W.; Yeager, E. *J. Appl. Electrochem.* **1989**, *19*, 19−27.
(14) Tian, J.; Morozan, A.; Sougrati, M. T.; Lefèvre, M.; Chenitz, R.; Dodelet, J. P.; Jones, D.; Jaouen, F. *Angew. Chem.* **2013**, *125*, 7005−7008.
(15) Choi, C. H.; Park, S. H.; Wooa, S. I. *Appl. Catal., B* **2012**, *119*−*120*, 123−131.
(16) Wu, G.; Chen, Z.; Artyushkova, K.; Garzon, F. H.; Zelenay, P. *ECS Trans.* **2008**, *16*, 159−170.
(17) Yin, J.; Qiu, Y.; Yu, J. *Electrochem. Commun.* **2013**, *30*, 1−4.
(18) Wu, G.; More, K. L.; Johnston, C. M.; Zelenay, P. *Science* **2011**, *332*, 443−447.
(19) Gong, K.; Du, F.; Xia, Z.; Durstock, M.; Dai, L. *Science* **2009**, *323*, 760−764.
(20) Bezerra, C. W.; Zhang, L.; Lee, K.; Liu, H.; Marques, A. L.; Marques, E. P.; Wang, H.; Zhang, J. *Electrochim. Acta* **2008**, *53*, 4937−4951.
(21) Li, X.; Liu, G.; Popov, B. N. *J. Power Sources* **2010**, *195*, 6373−6378.
(22) Yu, D.; Zhang, Q.; Dai, L. *J. Am. Chem. Soc.* **2010**, *132*, 15127−15129.
(23) Cheon, J. Y.; Kim, T.; Choi, Y.; Jeong, H. Y.; Kim, M. G.; Sa, Y. J.; Kim, J.; Lee, Z.; Yang, T. H.; Kwon, K. *Sci. Rep.* **2013**, *3*, 1−8.
(24) Ikeda, T.; Boero, M.; Huang, S. F.; Terakura, K.; Oshima, M.; Ozaki, J. i. *J. Phys. Chem. C* **2008**, *112*, 14706−14709.
(25) Carvalho, A.; Dos Santos, M. *J. Appl. Phys.* **2006**, *100*, 1−5.
(26) Tang, Y.; Allen, B. L.; Kauffman, D. R.; Star, A. *J. Am. Chem. Soc.* **2009**, *131*, 13200−13201.
(27) Zheng, Y.; Liu, J.; Liang, J.; Jaroniec, M.; Qiao, S. Z. *Energy Environ. Sci.* **2012**, *5*, 6717−6731.
(28) Wang, Y.; Wang, X.; Antonietti, M. *Angew. Chem., Int. Ed.* **2012**, *51*, 68−89.
(29) Thomas, A.; Fischer, A.; Goettmann, F.; Antonietti, M.; Müller, J. O.; Schlögl, R.; Carlsson, J. M. *J. Mater. Chem.* **2008**, *18*, 4893−4908.
(30) Chen, X.; Jun, Y. S.; Takanabe, K.; Maeda, K.; Domen, K.; Fu, X.; Antonietti, M.; Wang, X. *Chem. Mater.* **2009**, *21*, 4093−4095.
(31) Zhang, Y.; Liu, J.; Wu, G.; Chen, W. *Nanoscale* **2012**, *4*, 5300−5303.
(32) Chen, X.; Zhang, J.; Fu, X.; Antonietti, M.; Wang, X. *J. Am. Chem. Soc.* **2009**, *131*, 11658−11659.
(33) Lee, S. C.; Lintang, H. O.; Yuliati, L. *Chem.—Asian J.* **2012**, *7*, 2139−2144.
(34) Groenewolt, M.; Antonietti, M. *Adv. Mater.* **2005**, *17*, 1789−1792.
(35) Li, X.; Zhang, J.; Shen, L.; Ma, Y.; Lei, W.; Cui, Q.; Zou, G. *Appl. Phys. A: Mater. Sci. Process.* **2008**, *94*, 387−392.
(36) Dong, F.; Wu, L.; Sun, Y.; Fu, M.; Wu, Z.; Lee, S. C. *J. Mater. Chem.* **2011**, *21*, 15171−15174.
(37) Wang, X.; Chen, X.; Thomas, A.; Fu, X.; Antonietti, M. *Adv. Mater.* **2009**, *21*, 1609−1612.
(38) Sheng, Z. H.; Shao, L.; Chen, J. J.; Bao, W. J.; Wang, F. B.; Xia, X. H. *ACS Nano* **2011**, *5*, 4350−4358.
(39) Byon, H. R.; Suntivich, J.; Shao-Horn, Y. *Chem. Mater.* **2011**, *23*, 3421−3428.
(40) Lee, J. S.; Park, G. S.; Lee, H. I.; Kim, S. T.; Cao, R.; Liu, M.; Cho. *J. Nano Lett.* **2011**, *11*, 5362−5366.
(41) Mo, Z.; Peng, H.; Liang, H.; Liao, S. *Electrochim. Acta* **2013**, *99*, 30−37.
(42) Kwon, K.; Sa, Y. J.; Cheon, J. Y.; Joo, S. H. *Langmuir* **2012**, *28*, 991−996.
(43) Parvez, K.; Yang, S.; Hernandez, Y.; Winter, A.; Turchanin, A.; Feng, X.; llen, K. M. *ACS Nano* **2012**, *6*, 9541−9550.
(44) Liu, J.; Zhang, T.; Wang, Z.; Dawson, G.; Chen, W. *J. Mater. Chem.* **2011**, *21*, 14398−14401.
(45) Morozan, A.; Jégou, P.; Jousselme, B.; Palacin, S. *Phys. Chem. Chem. Phys.* **2011**, *13*, 21600−21607.
(46) Xiao, H.; Shao, Z. G.; Zhang, G.; Gao, Y.; Lu, W.; Yi, B. *Carbon* **2013**, *57*, 443−451.
(47) Velázquez-Palenzuela, A.; Zhang, L.; Wang, L.; Cabot, P. L. S.; Brillas, E.; Tsay, K.; Zhang, J. *J. Phys. Chem. C* **2011**, *115*, 12929−12940.
(48) Ren, Q. Z.; Huang, J. W.; Zhu, Z. A.; Ji, L. N.; Chen, Y. T. *J. Porphyrins Phthalocyanines* **2001**, *5*, 449−455.
(49) Zhang, Y.; Thomas, A.; Antonietti, M.; Wang, X. *J. Am. Chem. Soc.* **2009**, *131*, 50−51.
(50) Lee, C. L.; Huang, C. H.; Huang, K. L.; Tsai, Y. L.; Yang, C. C. *Carbon* **2013**, *60*, 392−400.
(51) Wakabayashi, N.; Takeichi, M.; Itagaki, M.; Uchida, H.; Watanabe, M. *J. Electroanal. Chem.* **2005**, *574*, 339−346.
(52) Wu, G.; Nelson, M.; Ma, S.; Meng, H.; Cui, G.; Shen, P. K. *Carbon* **2011**, *49*, 3972−3982.
(53) Lefèvre, M.; Proietti, E.; Jaouen, F.; Dodelet, J. P. *Science* **2009**, *324*, 71−74.
(54) Li, W.; Wu, J.; Higgins, D. C.; Choi, J. Y.; Chen, Z. *ACS Catal.* **2012**, *2*, 2761−2768.
(55) Nallathambi, V.; Lee, J. W.; Kumaraguru, S. P.; Wu, G.; Popov, B. N. *J. Power Sources* **2008**, *183*, 34−42.
(56) Oh, H. S.; Kim, H. *J. Power Sources* **2012**, *212*, 220−225.
(57) Deng D, H.; Yu, L.; Chen, X. Q.; Wang, G. X.; Jin, L.; Pan, X. L.; Deng, J.; Sun, G. Q.; Bao, X. H. *Angew. Chem., Int. Ed.* **2012**, *51*, 1−6.
(58) Shao-Horn, Y.; Sheng, W. C.; Chen, S.; Ferreira, P. J.; Holby, E. F.; Morgan, D. *Top. Catal.* **2007**, *46*, 285−305.